Design and system integration of the superconducting wiggler magnets for the Compact Linear Collider damping rings

Daniel Schoerling,[1,2] Fanouria Antoniou,[2] Axel Bernhard,[3] Alexey Bragin,[4] Mikko Karppinen,[2] Remo Maccaferri,[2] Nikolay Mezentsev,[4] Yannis Papaphilippou,[2] Peter Peiffer,[3] Robert Rossmanith,[3] Giovanni Rumolo,[2] Stephan Russenschuck,[2] Pavel Vobly,[4] and Konstantin Zolotarev[4]

[1]*Technische Universität Bergakademie Freiberg, Germany*
[2]*CERN, Switzerland*
[3]*KIT, Karlsruher Institute of Technology, Karlsruhe, Germany*
[4]*Budker Institute of Nuclear Physics SB RAS, Novosibirsk, Russia*

(Received 5 December 2011; published 24 April 2012)

To achieve high luminosity at the collision point of the Compact Linear Collider (CLIC), the normalized horizontal and vertical emittances of the electron and positron beams must be reduced to 500 and 4 nm before the beams enter the 1.5 TeV linear accelerators. An effective way to accomplish ultralow emittances with only small effects on the electron polarization is using damping rings operating at 2.86 GeV equipped with superconducting wiggler magnets. This paper describes a technical design concept for the CLIC damping wigglers.

DOI: 10.1103/PhysRevSTAB.15.042401 PACS numbers: 84.71.Ba, 41.20.Gz, 41.75.Ht

I. INTRODUCTION

The Compact Linear Collider (CLIC) is a study for an electron-positron collider in the TeV range. Fundamental physics data complementary to the Large Hadron Collider (LHC) and lower-energy linear electron-positron colliders may be obtained with measurements at the collision point of CLIC. Detailed information on the CLIC design study can be found in [1].

To achieve the required luminosity at the collision point of CLIC, the normalized horizontal emittance including the effect of intrabeam scattering (IBS) has to be less than 500 nm rad before entering the linear collider. Intrabeam scattering is a small angle multiple Coulomb scattering effect [2], which causes a beam emittance growth. Moreover, the normalized vertical zero-current emittance has to be 4 nm rad and the normalized longitudinal zero-current emittance has to be 6000 eV m. For the reduction of the emittance, damping rings are foreseen. Both the electron and the positron beams enter first the predamping rings and afterwards the main damping rings. The damping rings will be racetrack shaped rings with 26 wigglers placed in each straight section. The horizontal equilibrium emittance is designed to be around 1 order of magnitude smaller than in other planned or built rings (Fig. 1), which can be only achieved with superconducting damping wiggler magnets.

The baseline design foresees Nb-Ti superconducting wigglers. But by using the more challenging Nb_3Sn technology the magnetic flux density amplitude B_w can be increased (see Fig. 2 for the parameters of the wiggler magnets), which may open the possibility to shorten the damping rings. Moreover, the enthalpy margin for Nb_3Sn wiggler magnets with the same loadline margin as Nb-Ti wiggler magnets is larger, which will result in more stable operation. The first promising tests show that Nb_3Sn wiggler magnets can reach the high magnetic flux density, but more detailed studies are required before a final decision can be taken.

To test the wiggler system with beam, two prototypes of two different concepts of superconducting wigglers are foreseen to be installed in the ANKA storage ring [3]. The operational parameters for Nb-Ti are: $B_w = 3.0$ T, 35 periods, 56 mm period length, a beam stay clear of 13 mm, and a magnetic gap g of 18 mm. The design values for a Nb_3Sn wiggler magnet are (except for the magnetic flux density which is $B_w = 4.0$ T) identical. The test of the Nb_3Sn damping wiggler can be performed in the same cryostat.

The schematic layout of the cryostat is shown in Fig. 3. The essential of the design is that the vacuum chamber and superconducting coils have minimum thermal contact and that they are cooled by using separate cooling circuits. In between the vacuum chamber and the coils is a small vacuum (10^{-4} Pa) gap. The vacuum chamber is spaced to the coils by using small spacers with a low thermal conductivity. So, if the vacuum chamber receives heat load from the beam, the coils are only slightly affected. The vacuum chamber with a vacuum level smaller than 10^{-7} Pa [4] is cooled by gaseous helium and can be operated at temperature levels between 20 and 80 K; cooling at 80 K would reduce the power consumption by about a factor of 5 compared to cooling at 20 K. For the

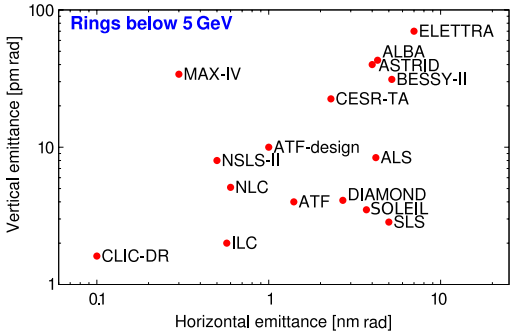

FIG. 1. Comparison of vertical versus horizontal emittances of different storage rings below 5 GeV with the CLIC damping rings [45].

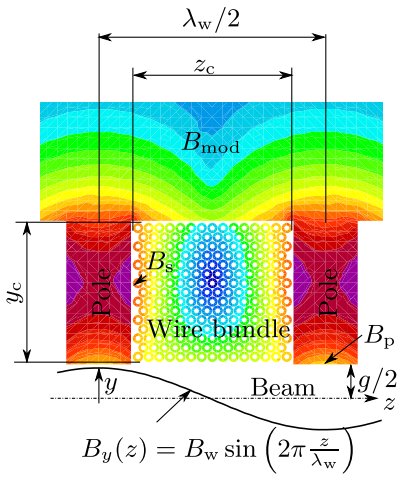

FIG. 2. Parameters of the wiggler magnets.

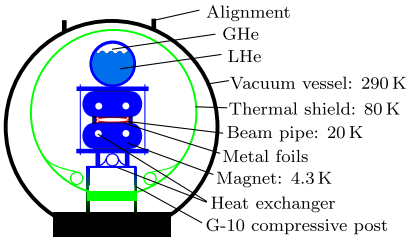

FIG. 3. Conceptual design of cryostat.

positron damping ring it might be additionally necessary to coat the vacuum chambers with specialized coatings to reduce electron cloud effects (see Sec. IV B 2). The coils are cooled by a flow of liquid helium at atmospheric pressure flowing through heat exchangers. This cooling technique reduces significantly the amount of stored helium. Since the liquid helium flows through the center of the coils, the existing coils act as a rigid mechanical barrier between the vacuum and the liquid helium. Therefore, no additional pressure barrier between coils and beam vacuum as in standard wiggler magnets with bath cooling (summarized in [5]) is needed to ensure that the beam pipe is not plastically deformed in the case of quench due to the mechanical load of the pressure increase caused by the vaporizing helium (usually up to 10^6 Pa). Therefore, the wiggler magnet with the proposed cooling system can be operated with the same beam stay clear but at a smaller pole distance resulting in a considerably larger magnetic field compared to bath cooled magnets because of the nonlinear magnetic flux density to gap relation given in Eq. (3).

In this paper, a conceptual design for superconducting vertical and horizontal racetrack damping wiggler magnets (see Fig. 4) is presented, which allows one to derive very quickly an optimized wiggler magnet design for damping rings. Moreover, a full analysis of the heat load in racetrack damping rings equipped with superconducting damping wiggler magnets in series in a racetrack damping ring is derived. The heat load analysis shows that conduction cooling has to be applied to superconducting wiggler magnets. So far, to the knowledge of the authors, all existing superconducting damping wiggler magnets are cooled by using bath cooling. A design concept for conduction cooling is presented.

Design requirements

In the following section we discuss the choice of wiggler parameters and technology required to achieve the ultralow emittance. Both bending magnets and wiggler magnets contribute to the damping time and the emittances. A detailed general mathematical analysis of the dependence of the emittances and the damping times on the various parameters can be found in [6]. The concept and the list of the parameters for the CLIC damping rings can be found in [7,8]. Three effects are determining the equilibrium emittance.

(i) Excitation and damping occurs due to the emission of synchrotron radiation. The damping is based on the effect that emission of synchrotron radiation reduces both the longitudinal and the transverse momentum of the electron. However, the cavities only restore the longitudinal momentum leading to a reduction of the transverse momentum. The equilibrium emittance calculated by considering these two effects is called zero-current emittance.

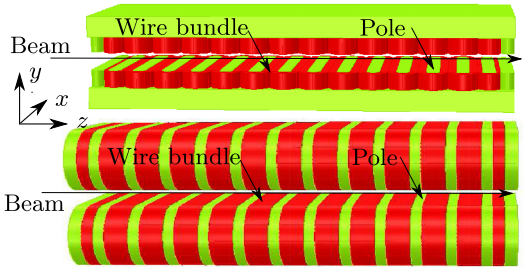

FIG. 4. Horizontal (top) and vertical (bottom) racetrack wiggler magnets.

(ii) Intrabeam scattering causes an increase of the zero-current emittance (determined by the effects mentioned above) due to small angle multiple Coulomb scattering.

The physical analysis of damping and excitation, without considering the effect of intrabeam scattering, allows the following conclusions to be drawn: in order to make the wiggler section as short as possible, the magnetic flux density B_w has to be large. Also the damping time τ is shorter the larger B_w is. But a high wiggler magnetic flux density B_w only produces low emittances when the product of $|B_w^3|$ and the period length λ_w^2 is small. Therefore, the ideal damping ring has wigglers with a large magnetic flux density B_w at a short period length λ_w.

However, the effective emittance in the ring will be larger than the zero-current emittance because of the effect of intrabeam scattering. The final normalized emittance of the beam $\gamma\epsilon_u$, with $u = x, y, z$ is given by

$$\gamma\epsilon_u = \gamma\epsilon_{u,0} + \gamma\epsilon_{u,\mathrm{IBS}}. \tag{1}$$

The normalized emittance growth from intrabeam scattering is proportional to the brightness of the beam, that is,

$$\gamma\epsilon_{u,\mathrm{IBS}} \propto \frac{N^Q}{\epsilon_x^{b_1}\epsilon_y^{b_2}\epsilon_z^{b_3}}, \tag{2}$$

where N is the number of particles per bunch and $\{Q, b_1, b_2, b_3\}$ is a set of positive real numbers. The effect of intrabeam scattering in existing rings is small, but in the first design studies [7] of the CLIC damping rings, the magnitude of the final emittance was dominated by intrabeam scattering. Therefore, in [2] the damping rings were reoptimized such that $\gamma\epsilon_x/\gamma\epsilon_{x,0} \leq 1.9$.

Figure 5 shows the calculated emittance taking into account all the previously mentioned effects for beam energies between 2 and 4 GeV. The emittances have a broad minimum between 2 and 3 GeV. From Fig. 5, an energy of 2.86 GeV was chosen. A more detailed analysis can be found in [2].

In the next step, B_w and λ_w for the damping wigglers have to be specified.

The maximum achievable flux density strength B_w as a function of the gap to period length ratio g/λ_w and the pole magnetic flux density B_p can be derived in free space from Maxwell's magnetostatic equations:

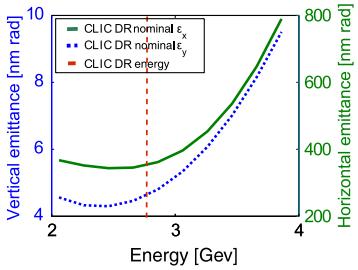

FIG. 5. Vertical and horizontal normalized emittances versus beam energy [2].

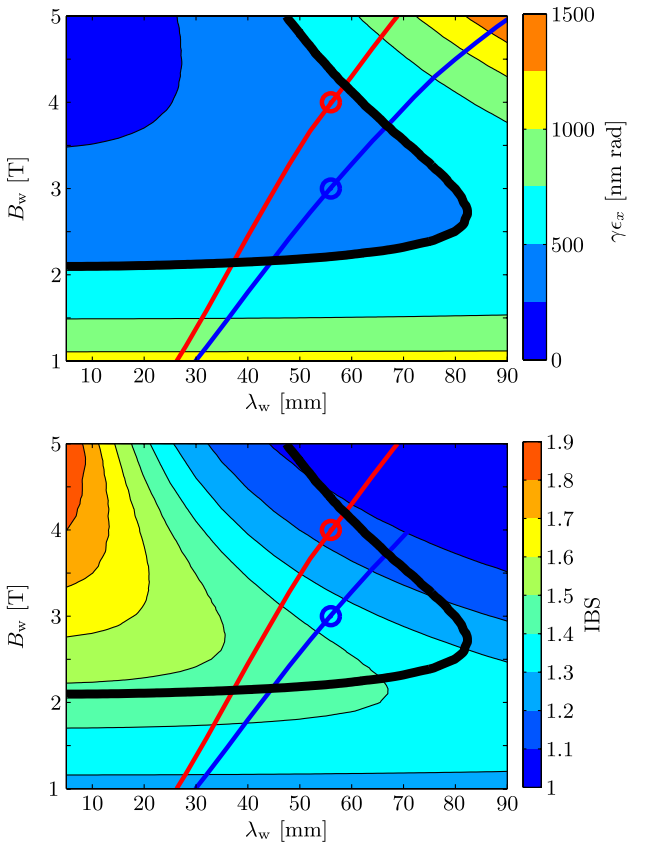

FIG. 6. Equilibrium normalized horizontal emittance $\gamma\epsilon_x$ (top) and the effect of IBS ($\gamma\epsilon_x/\gamma\epsilon_{x,0}$). The red and the blue curves show the maximum achievable magnetic flux density for superconducting wiggler magnets with Nb_3Sn and Nb-Ti wire technology, respectively.

$$B_w = \frac{B_p}{\cosh(\pi\frac{g}{\lambda_w})}, \tag{3}$$

where B_p is the pole field on the iron (see Fig. 2).

The gap of superconducting wiggler magnets is determined by the required aperture and space to intercept the heat and radiation load from the beam. An aperture of 13 mm is foreseen in the damping rings. To intercept the heat and radiation load from the beam, 2.5 mm space on each side is required. Therefore, the magnetic gap was set to 18 mm for these calculations.

The normalized horizontal and vertical emittances have to be predamped from 100 μm rad for electrons and 9.7×10^3 μm rad for positrons to 63 μm rad (horizontal) and 1.5 μm rad (vertical) in predamping rings [9]. For the emittance calculations the normalized vertical zero-current emittance was set to 4 nm rad, and the normalized longitudinal zero-current emittance was set to 6000 eV m. The total wiggler length in one ring was set to 104 m. Figure 6 shows the results of this study. Figure 6 (top) shows the normalized horizontal emittance as it is the most critical and can be used to decide on the required wiggler parameters. The red and the blue curves show the maximum

TABLE I. Parameters of wiggler magnet prototypes. HR: horizontal racetrack; VR: vertical racetrack.

	Nb-Ti HR	Nb_3Sn VR
Short sample		
B_w	3.6 T	5.5 T
Maximum stored E	80 kJ	700 kJ
I_c at B_w	740 A	1250 A
B_s at B_w	6.3 T	9.9 T
Operational parameters		
B_w^d	3.0 T	4.0 T
T_c^d	5.1 K	11.9 K
I^d	630 A	855 A
B_s^d	5.4 T	6.7 T
Operation T	4.2 K	4.2 K
Gap	18 mm	18 mm
λ_w	56 mm	56 mm
K	15.7	20.9
Strand	Bochvar Institute [10]	OST RRP [11]

achievable field for superconducting wiggler magnets with Nb_3Sn and Nb-Ti wire technology, respectively. The red and the blue points present the proposed Nb_3Sn and Nb-Ti working points. The parameters of the wiggler magnets represented by these points are presented in Table I. Figure 6 (bottom) presents the effect of intrabeam scattering on the normalized emittance, for example a value of 1.2 means that 20% of the emittance is generated by the effect of IBS.

Figure 6 (top) shows that only wigglers with a period length λ_w of less than 80 mm and with a sinusoidal wiggler field with a magnetic flux density amplitude B_w larger than 2.2–2.5 T fulfill the requirements of the CLIC damping rings. For period lengths λ_w of 50 to 80 mm and magnetic flux densities B_w of 2.8–4.5 T, the effect of intrabeam scattering [Fig. 6 (bottom)] can be minimized.

In the prototype phase the wiggler magnets will be tested in the ANKA storage ring and will also be used as a light source. Therefore, a smaller period length λ_w was chosen to satisfy the needs of both ANKA and CLIC. The Nb-Ti wiggler magnet will be operated at 85% and the Nb_3Sn wiggler magnet at 68% of the critical current. The loadline margin for Nb_3Sn was chosen larger for additional margin because the manufacturing and operation of Nb_3Sn wiggler magnets is purely R&D. Each of the 104 superconducting wiggler magnets has 34 periods. 26 wigglers will be installed in each of the straight sections of the two damping rings. This discussion shows that the development of short-period superconducting wiggler magnets with a high magnetic flux density strength B_w and small gap g is required.

Hybrid-permanent wiggler magnets are not able to reach the required large magnetic flux densities. The magnetic saturation induction of iron ($B = 2.15$ T) can be considered as the theoretical upper limit for the pole field of hybrid-permanent magnet wigglers.

II. WIGGLER MAGNET DESIGN

In this section we present a conceptual design for superconducting wiggler magnets. From the requirements of the CLIC damping rings, the gap size g, the period length λ_w, and the minimal required magnetic flux density in the center of the gap B_w are assumed to be given. The choice of the wiggler coil design, the choice of the strand technology (Nb-Ti or Nb_3Sn), and the choice of the wire bundle dimension are discussed in the following. Further on, in the case of vertical wiggler magnets, the bending radii of the end coils have to be determined. The parameters required for the optimization are summarized in Table II and illustrated in Fig. 2, where B_w refers to the amplitude of the magnetic flux density, B_p to the pole field, and B_s to the surface field on the conductor. We chose not to investigate the graded coils (coils with changing engineering current density over the wire bundle) because they require the use of multiple power supplies and current leads. All magnetic calculations were performed by using the OPERA software package [12].

We assume that the design parameters B_w^d, λ_w^d, and g^d are given; the design pole field B_p^d can be directly calculated by using

$$B_p^d = B_w^d \cosh \pi \frac{g^d}{\lambda_w^d}. \tag{4}$$

Figure 7 (top) can be used to find the required engineering current density J_{eng}^* from the intersection of $B_p^d = B_p^*$ and the design period length $\lambda_w^d = \lambda_w$, where $*$ denotes the maximum achievable pole field B_p^* for a period length λ_w at the engineering current density J_{eng}^*. In this first step of the optimization, the design pole field B_p^d is set to the maximum achievable pole field B_p^* for a given period length λ_w at the engineering current density J_{eng}^*. In Fig. 7 a gap of 18 mm was assumed, which can be adjusted by using Eq. (4).

After determining the required engineering current density J_{eng}^* for the desired pole field in Fig. 7 (top), $B_p^d = B_p^*$; the maximum field on the conductor B_s^* can be read off from the intersection of J_{eng}^* and the period length λ_w in Fig. 7 (bottom). If the intersection point of J_{eng}^* and the period length λ_w^* are below the critical surface shown for Nb-Ti (Bochvar Strand) or Nb_3Sn (OST RRP) it can be, in principle, realized.

If a strand is used that is different from the two shown in Fig. 7, the engineering current density has to be converted correspondingly into the current in the strand with

TABLE II. Nomenclature.

B_w^*	Maximum achievable field at λ_w
B_p^*, B_s^*, I_c^*, J_{eng}^*	Corresponding values at B_w^*
B_p^d, B_s^d, I^d, g^d, λ_w^d	Design operating values

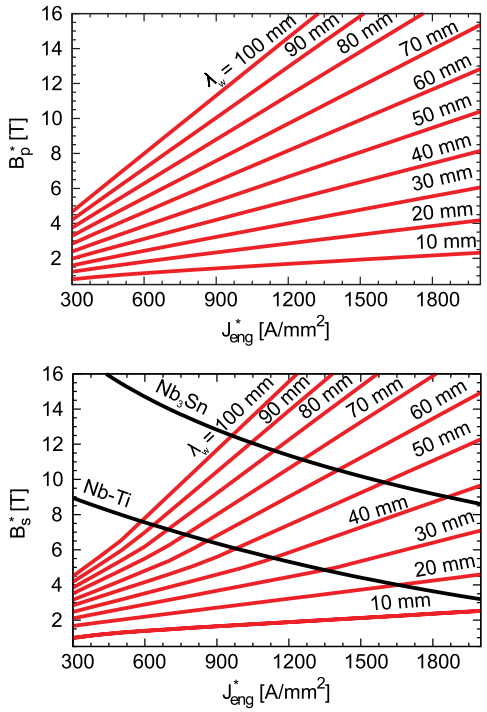

FIG. 7. Top: Optimized field at the pole tip B_p^* versus engineering current density. Bottom: Load lines for wiggler magnets with a coil width ($0.3\lambda_w = y_c = z_c$) and a gap 18 mm. For example, in the bottom plot, we find that an engineering current density $J_{eng}^* = 975$ A mm^{-2} yields a maximum surface field $B_s^* = 6$ T for a Nb-Ti strand at a period length $\lambda_w = 50$ mm. The top plot shows that this wiggler configuration would yield a maximum pole field $B_p^* = 5.5$ T.

$$I = \frac{1}{\kappa} J_{eng}, \tag{5}$$

where we define the filling factor κ for the wiggler magnets as the average number of wires per unit area. For the calculations presented here, a filling factor of 1.24 strands/mm^2 was assumed. As Fig. 7 reveals, $B_p \propto J_{eng}$. Therefore, the part of the coil generating the field seen by the beam must be densely wound. In vertical wiggler magnets, the layer jump can be conveniently placed on the side averted from the beam. In horizontal racetrack coils, usually the layer jump is placed in the straight part, resulting in an around 10% smaller filling factor compared to that of vertical wiggler magnets.

We have to introduce the critical surface in order to determine if the chosen strand is superconducting at the chosen B_s [shown for the two sample strands in black in Fig. 7 (bottom)]. A superconducting filament in a magnetic field is superconducting as long as the current is smaller than the critical current. For a Nb-Ti strand, the critical current is [13]

$$I_c = C B_s^{\alpha-1}\left(1 - \frac{B_s}{B_{c2}(T)}\right)^{\beta}. \tag{6}$$

For the Nb-Ti Bochvar Institute strand, $C = 3300$, $\alpha = 0.72$, $\beta = 1.1$, and $B_{c2}(4.2) = 10.68$. For a Nb_3Sn strand, the critical current is [14,15]

$$I_c = \frac{C}{\sqrt{B_s}}\left(1 - \frac{B_s}{B_{c2}(T, \epsilon)}\right)^2. \tag{7}$$

For the OST RRP 0.8 mm strand, $C = 11\,030$, $B_{c2}(4.2, 0) = 24.92$.

In vertical racetrack wigglers, the bending radius can be chosen at will. It is useful to choose it in a way that the Lorentz force acting on the wire bundle is compressive. Figure 8 shows the bending radii for Nb-Ti and Nb_3Sn wiggler magnets at which the force becomes zero. For larger bending radii, the Lorentz force is compressive; for smaller bending radii, the Lorentz force is tensile. In horizontal racetrack wiggler magnets this option obviously does not exist because the bending radii are given by the pole width. Because the pole width is much smaller than the radii shown in Fig. 8, the Lorentz forces in the end coils of horizontal wiggler magnets are tensile. In the straight section, the wire bundles are compressed towards the unsaturated iron. If no iron is used, the forces will be tensile. A yoke on top of a vertical wiggler magnet reduces the resulting force on the wire bundles on the upper straight part. One has to be careful at the first and last coils of the wiggler magnets. Forces acting away from the wiggler body occur and have to be supported by an adequate mechanical structure.

Wiggler magnets have to be transparent for the beam. That means, the first and second field integrals

$$I_y = \int_{s_0}^{s_1} B_y(z) dz, \tag{8}$$

$$II_y = \int_{s_0}^{s_1} \int_{s_0}^{s} B_y(z') dz' dz, \tag{9}$$

over the wiggler magnet have to vanish. Two different designs are commonly used to compensate the first and the second field integral, either a symmetric (odd number of poles) or an antisymmetric (even number of poles) design. In superconducting wiggler magnets the

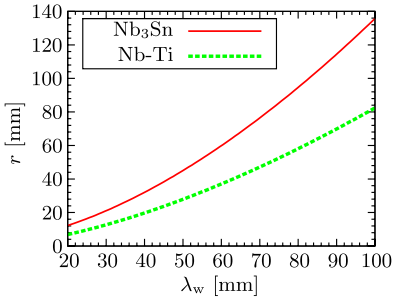

FIG. 8. Optimized end-coil radius r for Nb-Ti and Nb_3Sn wiggler magnets with zero force in the end coil.

antisymmetric design is preferred. The first field integral automatically becomes zero and reduces the possibility of beam trips in the case of a quench [16]. Further, the integrals of the higher even multipoles (sextupole, decapole, ...) are canceled automatically because they are equal in size but different in sign. The second field integral has to be minimized by varying the number of conductors or the geometry of the last coils by using a numerical calculation method. If the magnet is operated at different current levels, the first and the last pole should be thick enough to not saturate.

In the last paragraph, we saw that all even multipoles are canceled automatically. Finally, we have to ensure that the influence of the odd numbered multipoles (quadrupoles, octupoles, ...) remains also acceptably small. Tolerances for the dynamic field integral $\int B_y ds$ have to be determined by performing tracking studies to specify the allowable range, where s denotes the trajectory of the particles. It is shown in [17] that it is not sufficient to consider $\int B_y dz$, where z follows the global coordinate of the overall beam direction. The good-field region is defined as the region where the relative change in magnetic flux density is less than 1×10^{-4}. Figure 9 shows this region for typical wiggler designs. The maximum deflection of the beam in a wiggler magnet in the CLIC damping rings is $x = 2.65 \times 10^{-3} B_w \lambda_w^2$, where all values have to be entered in SI units. For $B_w = 3$ T we find around ± 30 μm. The beam size is smaller than 1.2 mm. We suggest to choose a good-field region of at least 4 mm.

The final step in the magnet design of a superconducting wiggler is the quench analysis. A quench is a transition from the superconducting to the normal-conducting state followed by a thermal runaway. When the superconductor becomes normal conducting, the current flows through the stabilizing copper of the strand causing resistive heating of the magnet, which has to be switched off. Wigglers can be built and protected in modules; in the extreme, each half period can be protected separately by means of a parallel resistor within the magnet coldmass, as it was done for the LHC beam diagnostics undulator [18]. If a coil of the wiggler quenches, the parallel resistor acts both as energy extraction for the quenched coil and bypass for the current. This protection scheme is feasible because the stored energy in a single coil of a wiggler magnet is relatively small

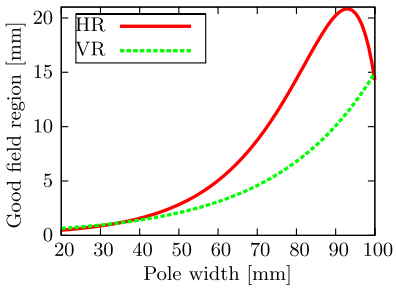

FIG. 9. Example of rolloff of wiggler magnets ($\lambda_w = 56$ mm).

(< 10 kJ). A PSPICE simulation was performed. As input parameter the resistance increase value after the occurrence of a quench was extrapolated from the CERN-KIT short-model wiggler (Sec. III). The analysis has shown that even the protection of many wiggler magnets powered in series is feasible.

A. Influence of field errors

Magic fingers magnetic shims can be used to compensate both for small errors of the first and the second field integrals and for small multipole errors due to mechanical errors in the wiggler magnets [17]. Additional steerers can be used for compensation of the field integrals.

The horizontal equilibrium emittance and the damping time [6] without considering the effect of intrabeam scattering vary less than 5% over a hypothetical, 1×10^6 damping rings with Gaussian distributed errors of the magnetic flux density amplitude B_w and period length λ_w. The standard deviation for this study was set to: $\sigma(B_w) = 0.2$ T and $\sigma(\lambda_w) = 1$ mm. A standard deviation of $\sigma(B_w) = 0.2$ T corresponds to an error in the pole height of ± 1.5 mm if $B_p = \text{const}$ and $\lambda_w = \text{const}$. These tolerances can be easily achieved. Therefore, no special care has to be taken to maintain small tolerances during the manufacturing of the wiggler magnets.

Notice that if the yaw, pitch, or roll angles obtained with magnet alignment do not meet the target values, higher-order field components are introduced which are not represented in the field model described above.

B. Temperature level of SC coils

The operation at 1.9 K instead of 4.3 K increases the performance of a Nb-Ti wiggler by around 20% ($\lambda_w = 56$ mm). However, a Nb_3Sn wiggler with currently tested strands reaches almost the same B_w at 4.3 and 1.9 K due to self-field instabilities. Only the latest Nb_3Sn strand development may reach larger currents at 1.9 K [19]. Cooling at around 4.2 K can be economically provided by standard cryocoolers. Therefore, cooling at 1.9 K is not pursued. The power consumption at 1.9 K would be above 200 kW instead of 76.9 kW and could not be provided by cryocoolers (Sec. IV).

The wire bundle shown in Fig. 2 is encased in epoxy resin. Therefore, the superfluid helium cannot come in direct contact with the superconducting wire. As a result, the large thermal conductivity of superfluid helium at 1.9 K is only of limited advantage. Therefore, we choose to operate the wiggler magnets at 4.2 K, which eases cooling considerably and allows for cooling the wiggler magnets with cryocoolers.

III. CONCEPTUAL DESIGN VERIFICATION

Two Nb-Ti vertical racetrack short models were successfully manufactured and tested in two independent

TABLE III. Parameters of short models.

	CERN-KIT	CERN-BINP
Period, mm	40	50
Stored energy, kJ	1	10
Gap, mm	16	20
B_w, T at 4.2 K	1.9	2.2
B_w, T at 1.9 K	2.4	...
I_c at 4.2 K, A	730	700
B_s at 4.2 K, T	4.8	6.5
I_c at 1.9 K	910	...
Cu/Sc ratio	1.8/1	1/1.5
# poles	6	8
Strand	LHC #3 [21]	Bochvar Institute [10]

collaborations. In the framework of the CERN collaboration with the Karlsruhe Institute of Technology (KIT), Germany, a 40 mm period, Nb-Ti short model was manufactured reaching up to 2.4 T at 1.9 K. The magnet reached short sample current after 13 quenches. The results are published in [20]. In the framework of the CERN-Budker Institute of Nuclear Physics (BINP), Russia, collaboration, Nb-Ti short models with a period length of 50 mm were manufactured reaching up to 2.2 T at 4.2 K. The magnet reached short sample current after 20 quenches. The parameters of the two successfully tested short models are summarized in Table III. These tests have proven that Nb-Ti wiggler magnets in the proposed parameter space can be manufactured and operated.

IV. THERMAL DESIGN

This section presents a thermal design for the CLIC damping wigglers. It will be the first time that 26 superconducting wiggler magnets will be operated in one straight section. In this chapter we address the challenges related to this operation mode. For all following calculations the baseline parameters were used. The wiggler baseline design is the Nb-Ti HR design presented in Table I (left column). The baseline energy of the CLIC damping rings is 2.86 GeV.

A. Magnetically and electrically induced heat loads

Eddy currents will occur due to the varying magnetic flux density during the ramp-up or a quench of the wiggler magnets. For the test device in the ramping time is crucial, because during injection the wiggler has to be shut down. Therefore, the test device will be built by using laminated iron to minimize eddy currents during the ramp-up.

Resistive joints cannot be avoided. The horizontal racetrack wiggler magnets will have around 75 joints per meter wiggler length. Table IV summarizes the achieved resistance values normalized to a 1-cm overlap length. Cold welded Nb-Ti filament joints lead to the smallest resistances:

TABLE IV. Comparison of different joint technologies [22,23].

	Electrolytic Cu	Soldered	US welded	Cold welding
Nb-Ti	20 nΩ cm	40 nΩ cm	8 nΩ cm	<1 pΩ cm
Nb_3Sn	20 nΩ cm	40 nΩ cm	...	<10 nΩ cm

$$\frac{P}{L} < \frac{nRI^2}{L} < 1\frac{\mathrm{mW}}{\mathrm{m}}, \tag{10}$$

where P is the power, L the length of the wiggler, n the number of joints, R the resistance of one joint, and I the current in the strand. In the case of vertical racetrack wiggler magnets, the only joints are the interconnections to the current leads. This would yield for 4 interconnections operated at 855 A approximately 15 mW heat load.

B. Beam induced heat loads

1. Image currents

In [24] the anomalous skin effect was measured for metals with a small resistance at high frequencies. In this regime Ohm's law can no longer be applied because the free path of the conduction electrons is similar to the penetration depth of the electric field [25].

At cryogenic temperatures the electrical resistivity of pure metals such as OFHC copper is up to a factor of 300 lower than at room temperature. Therefore, the average power deposition per unit length due to the wakefield of the beam in the extreme anomalous skin effect regime of a cold beam pipe for aluminum or copper (coating) is given by [26]

$$P/L = \frac{\Gamma(\frac{5}{6})cZ_0}{4b\pi^2}\frac{I_{\mathrm{av}}^2}{\sigma_z^{5/3}\eta f_{\mathrm{rf}}}B_{\mathrm{mat}} \approx 1\frac{\mathrm{W}}{\mathrm{m}}. \tag{11}$$

The presented values for the image current power deposition were calculated with the values defined and given in Table V.

While good conductors do enter the anomalous skin effect regime at cryogenic temperatures and high frequencies, poor conductors do not. For poor conductors such as uncoated stainless steel or TiZrV ternary alloy, called nonevaporable getter (NEG) coating, the heat load can be estimated by normal skin effect formulas:

$$P/L = \frac{\Gamma(\frac{3}{4})c\sqrt{Z_0}}{\sqrt{32}b\pi^2}\frac{I_{av}^2}{\sigma_z^{3/2}\eta f_{\mathrm{rf}}}\frac{1}{\sqrt{\sigma_c}} \gtrsim 32\frac{\mathrm{W}}{\mathrm{m}}. \tag{12}$$

A material with poor conductivity is not acceptable because of its high heat load. Therefore, all the following calculations assume a high-conductivity material for the beam pipe.

TABLE V. Parameters for image current calculations, see Eqs. (11) and (12); parameter values from [8,26].

Parameter	Value	Unit	Explanation
$\Gamma(\frac{5}{6})$	1.13		Gamma function
B_{Al}	3.3×10^{-7}	$\mathrm{m}^{2/3}$	Material constant, Al
B_{Cu}	3.9×10^{-7}	$\mathrm{m}^{2/3}$	Material constant, Cu
σ_c	2×10^{6}	Sm^{-1}	Stainless steel conductivity (4.3 K)
Z_0	120π	Ω	Free space impedance
c	3×10^{8}	$\frac{\mathrm{m}}{\mathrm{s}}$	Speed of light
I_{av}	0.15	A	Average current
b	5.5×10^{-3}	m	Beam-pipe radius (reduced)
σ_z	1.4×10^{-3}	m	Bunch length
ηf_{rf}	$0.22 \times 1 \times 10^{9}$	Hz	Fraction of the ring circumference occupied by a bunch train for 1 GHz
	312		Number of bunches (2 trains $\times$ 156 bunches)
	4.1×10^{9}		Bunch population
	420	m	Ring circumference
	1.4×10^{-6}	s	Orbital period
	10^{-9}	s	Bunch separation

2. Electron clouds

The heat load estimation due to electron clouds in the electron and positron damping rings were performed with the ECLOUD code [27]. Figure 10 (top) shows the heat load induced by electron clouds in the electron damping ring. Multipacting is a phenomenon of resonant electron multiplication in which a large number of electrons is built up, leading to remarkable power losses, heating of the beam pipe and beam instabilities [28]. The electron beam is not affected by multipacting for values of a secondary electron emission yield δ_{max} up to 2.4.

In the positron ring, multipacting appears for a secondary electron emission yield $\delta_{\mathrm{max}} > 1.3$ and causes significantly stronger e-cloud effects over one train passage for values above 1.4–1.5; see Fig. 10 (bottom). As electron clouds cause not only heat load but also beam instabilities, low secondary electron emission yield coating is needed for the positron damping ring. The needs for the beam-pipe coating to avoid heating from e-clouds and from image currents are contradictory, because a large electron emission yield means usually a low resistivity of the beam-pipe coating. A thin-film low-secondary-yield coating may be sufficient to reduce the secondary electron emission, such a thin-film coating may not decrease the beam-pipe conductivity; surface treated grooved copper or amorphous carbon might be another solution [29]. The effect of e-cloud at low emittance rings is studied in detail at CesrTA [30].

3. Synchrotron radiation

Most synchrotron radiation generated in the damping wigglers has to be absorbed at ambient temperature to avoid heating of the superconducting coils. Figure 11 shows the principle of synchrotron radiation emission and absorption. The radiating charged particle is moving on a sinusoidal trajectory in the horizontal xz plane. The angles of observation in horizontal and vertical directions are θ and ψ. The emitted light, which will not be absorbed by upstream absorbers (yz plane), shown in cones, will

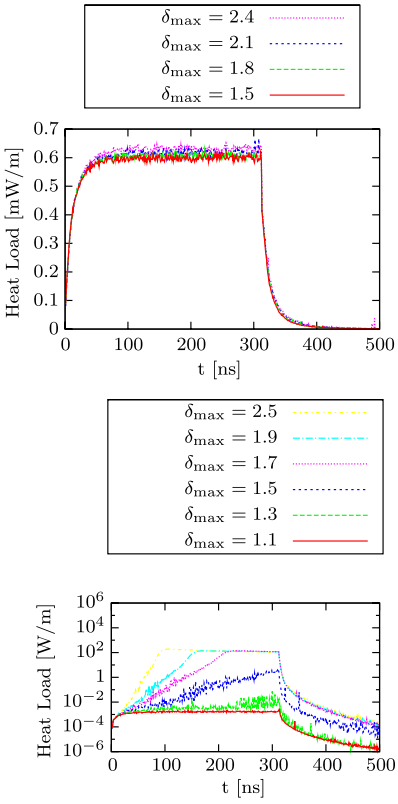

FIG. 10. Heat load induced by electron clouds in the electron damping ring (top). Heat load induced by electron clouds in the positron damping ring (bottom).

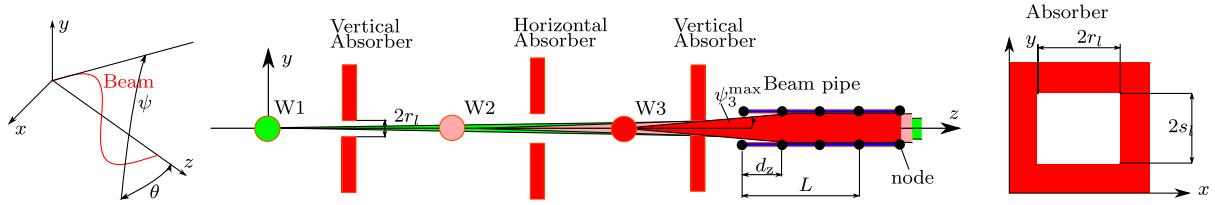

FIG. 11. Principle of synchrotron radiation emission (left), absorber scheme (middle), and absorber layout (right).

partly irradiate the beam pipe. As an example $\psi_3^{\max}$ is shown, the maximum angle at which wiggler W3 can irradiate synchrotron radiation on the beam pipe. The heat load on the beam pipe is calculated on nodes, which are equidistantly spaced. In this example only the synchrotron radiation of the two last wigglers can hit the beam pipe. Rectangular absorbers are proposed, because of manufacturing constraints. The power emitted from wiggler magnets is mainly concentrated within a light cone of small opening angle $K/\gamma \approx 3$ mrad, where K is the wiggler's deflection parameter and γ is the relative energy. However, the distance between the first wiggler and the last wiggler is around 80 m, which implies that a large part of the generated synchrotron radiation would irradiate the beam pipes of the upstream superconducting wigglers. A detailed mathematical description of the calculation method is given in Appendix A.

The heat load depends on the distance between the absorbers and therefore on the wiggler length (Table VI). From Table VI results the choice of 2 m long wiggler magnets, because the heat load from synchrotron radiation increases rapidly. Shorter wiggler magnets are not chosen, because each cryostat requires an approximately 2 times 0.5 m long cold-warm transition which reduces the compactness of the ring. The corresponding lattice design is presented in Table VII.

Figure 12 shows the heat load distribution on the beam pipe of the two last installed wiggler magnets (number 25 and 26) downstream of absorbers installed after quadrupoles aligned with their focusing planes. The horizontal aperture of the wiggler has to be large enough to reduce the heat load from synchrotron radiation (Table VIII). Figure 13 shows the contribution of each wiggler to the total heat load on the last and next-to-last wigglers. The total heat load from synchrotron radiation on the beam pipe downstream of a vertical absorber is less than 2 W and around 40 W downstream of a horizontal absorber. The first six wiggler magnets in the straight section of the damping rings are subject to less heat load.

TABLE VI. Heat load on last wiggler beam pipe after a horizontal absorber for different wiggler lengths L.

L, m	1	2	3	4	5	6
P, W	7	40	120	280	560	980

4. Absorption of synchrotron radiation in the beam pipe

The critical photon energy ϵ_c of the CLIC damping wiggler can be calculated according to [31]

$$\{\epsilon_c\}_{\mathrm{keV}} = 0.665\{E\}^2_{\mathrm{GeV}}\{B_{\mathrm{w}}\}_{\mathrm{T}} \approx 16 \text{ keV}. \quad (13)$$

The spectral intensity decreases rapidly for photon energies above ϵ_c.

The measured intensity I transmitted through a layer of material with thickness l is related to the initial intensity I_0 according to the Beer-Lambert law [32]:

$$\frac{I(l)}{I_0} = e^{-\mu l}, \quad (14)$$

where l denotes the penetration depth. The attenuation coefficient is μ. If we limit the transmitted energy to 1% of the initial intensity, the penetration depth can be calculated by $l_{1\%} = 4.6\frac{1}{\mu}$. For a photon energy of $3\epsilon_c \approx 50$ keV, the attenuation coefficients for common beam-pipe materials and the corresponding penetration depths are given in Table IX. The maximum penetration depth $l_{\max}$ at the full radiation cone opening angle, shown in Fig. 14, is also given in Table IX. It was assumed that the synchrotron radiation changes the angle to the beam axis when entering the vacuum chamber by Snell's law. In the following, it was assumed that this angle changes by a factor of 5.

TABLE VII. Lattice for heat load calculation of synchrotron radiation.

Element	Length, m	$2s_l$, mm	$2r_l$, mm	Shape
Horizontal absorber				
Wiggler	2	13	80	Elliptical
Transition and quadrupole	0.25	13	80	Elliptical
Absorber	0.5	13.5	12.3	Rectangular
Transition	0.25	13	40	Elliptical
Vertical absorber				
Wiggler	2	13	80	Elliptical
Transition and quadrupole	0.25	13.5	40	Elliptical
Absorber	0.5	9.5	12.5	Rect.
Transition	0.25	13.5	40	Elliptical
Beam pipe (heat load)	2	13	80	Elliptical

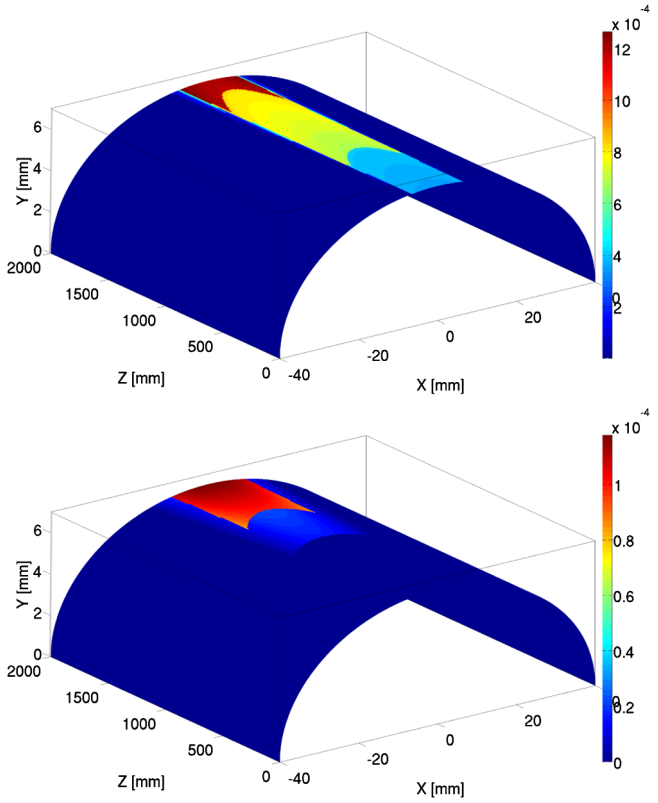

FIG. 12. Spatial distribution of synchrotron radiation on the beam pipe for the 25th wiggler with a total heat load of 40 W (top) and the 26th wiggler with a total heat load of 2 W (bottom) for the Nb-Ti baseline design (units: W/mm^2).

The maximum penetration depth is much smaller than the material thickness of the beam pipe (1 mm). Therefore, all synchrotron radiation will be absorbed in the inner part of the beam pipe and no heat will be deposited directly into the superconducting coils.

5. Absorber heat load

The absorber design was optimized such that the heat load on the vertical and horizontal absorbers is approximately balanced and reaches, after some 5 to 10 absorbers, its maximum value. Figure 11 shows the principle layout of the absorbers. They will be water cooled. After the last wiggler magnet, a dump will be installed to absorb the remaining synchrotron radiation. Figure 15 shows the heat load on each of the 26 absorbers.

A detailed mathematical description of the calculation method is given in Appendix B.

TABLE VIII. Heat load on the 25th beam pipe for different horizontal apertures (widths).

Width, mm	30	40	50	60	70	80
Heat load, W	62.8	47.9	43.1	40.9	39.6	38.9

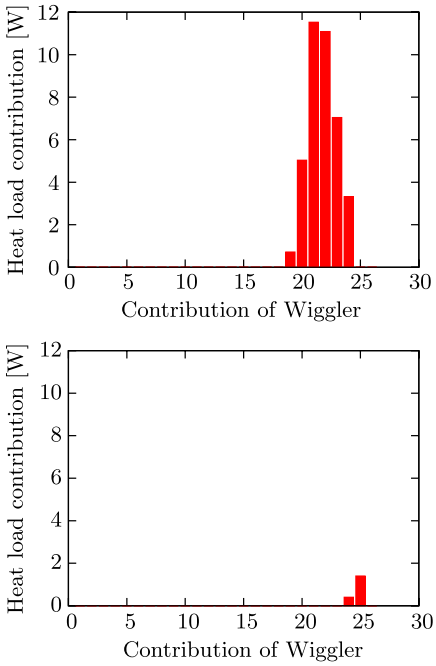

FIG. 13. Heat load on the 25th and 26th beam pipe of the wiggler magnets due to synchrotron radiation from upstream wiggler magnets.

C. Cooling concept and related heat loads

Figure 16 compares the standard cooling concept (bath cooling, left) with the cooling concept for the CLIC damping wigglers proposed in the introduction (indirect cooling, right, and Fig. 3). For indirect cooling the whole wiggler magnet is in an insulation vacuum. The helium is contained in the heat exchangers. In bath cooling the magnet is immersed in liquid helium (LHe). To extract the heat a copper liner cooled with gaseous helium contained in heat exchangers is required (depicted in red). Further, a mechanically stable pipe that can withstand the pressure increase during a quench (in black) is needed. This pipe also insulates the beam vacuum from the surrounding liquid helium. Although indirect cooling requires a detailed thermal design of the superconducting coils, it comes with a number of advantages compared to bath cooling: (i) mechanically less demanding beam pipe. Bath cooling would require a stainless steel beam pipe to sustain the pressure increase during a quench. Without this requirement, a 2 mm smaller gap can be realized, resulting in a more than 10% higher gap field B_w, (ii) less complex cryogenic

TABLE IX. Attenuation coefficients, densities, and penetration depths for a photon energy of 5×10^{-2} MeV [32].

Material	μ/ρ, $cm^2\,g^{-1}$	ρ, $g\,cm^{-3}$	μ, cm^{-1}	l, cm	l_{max}, μm
Al	0.3681	2.699	0.994	4.628	454
Cu	2.613	8.960	23.41	0.1965	19
Fe	1.958	7.874	15.42	0.298	29

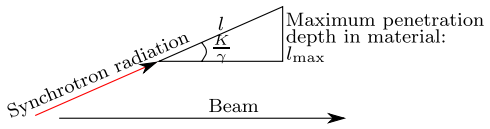

FIG. 14. Maximum penetration depth l_{max} of synchrotron radiation depending on the maximum opening angle of the radiation cone.

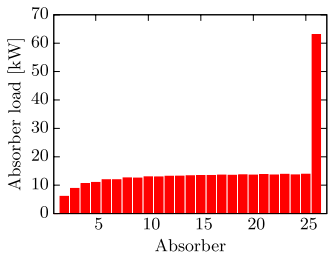

FIG. 15. Absorber load distribution including the dump at the end of the straight section.

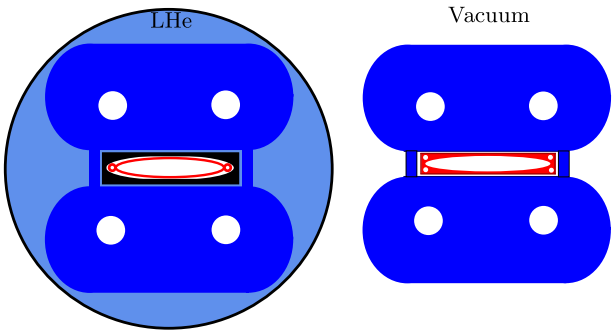

FIG. 16. Two cooling concepts. Left: Bath cooling. The magnet is immersed in liquid helium (LHe). Right: Indirect cooling. The whole wiggler magnet is in vacuum. The helium is contained in the heat exchangers.

structure because all helium is contained within the heat exchangers resulting in smaller helium mass, smaller valves, tubes, etc. (iii) cryostat design for exchangeable coils and vacuum pipes for maintenance and repairs is less complex.

An insulating vacuum of 10^{-4} Pa will be established to minimize the heat transfer to the superconducting coils by convection. The superconducting coils and the beam pipe will be mounted with minimal thermal contact and with materials such as glass-fiber reinforced plastics or Kevlar stripes with a large strength to heat conductivity ratio. All surfaces should be wrapped with polished well-conducting metal foils or aluminized Mylar foils with small emissivities to reduce heat transfer by radiation.

The temperature of the beam pipe will be stabilized at around 20 K where the heat conductivity k of copper is highest (Fig. 17) resulting in an isothermal beam

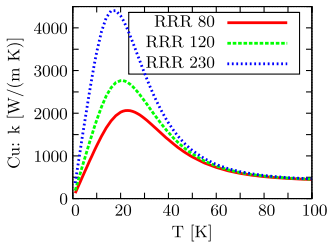

FIG. 17. Heat conductivity of OFHC copper versus temperature. Data from [46].

pipe. Cryocoolers for this temperature level are available, and radiation to the superconducting coils is kept to a minimum.

The heat load is deposited in the center of the cross section of the 2 m long beam pipe (Fig. 12) and has to be transported over $\lesssim 50$ mm to the outer side of the beam pipe. The resulting temperature difference is smaller than $\Delta T < \frac{1}{2}\frac{\dot{Q}l}{kA} \approx 0.3$ K, with the heat load $\dot{Q} = 50$ W, the distance from the center of the beam pipe to the heat exchanger $l = 50$ mm, the averaged heat conductivity $k = 2000\ \mathrm{W(m\,K)^{-1}}$ (RRR = 80), and cross section $A \geq 2 \times 10^{-3}\ \mathrm{m}^2$.

An overview of heat leak calculation methods for cryostats is given in [33–37]. The coils are in an insulation vacuum; therefore, the total heat load on the coils results mainly from conduction (current leads, and fixing structure) and is less than 1 W. Radiation and convection can be minimized by using a 60 to 80 K shield. No heat load induced by the beam is deposited directly into the coils because all heat load can be intercepted by a metallic beam pipe of a thickness of about 0.5 mm. The beam pipe can be cooled at a higher temperature level (20 K), which greatly reduces the consumed power for cooling. Table X gives a summary of all heat load sources occurring in the CLIC damping wigglers at the different temperature levels.

TABLE X. Summary of the average heat loads (all sources) at the different temperature levels in watts.

	Shield 80 K	Beam pipe 20 K	SC coils 4.2 K
Synchrotron radiation (HA)		40.0	
Synchrotron radiation (VA)		2.0	
Average synchrotron radiation		21.0	
Image currents		2.0	
E-clouds		0.02	
Radiation	16.3		0
Convection	1.0		0.10
Conduction	0.9		0.64
Joints	...		0.02
Current leads	72.0		0.16
Total (average)	90.2	23.0	0.9

TABLE XI. Power consumption of the cryogenic plants at the different temperature levels. The total power consumption is around 450 kW.

Temperature level, K	80	20	4.2
Total heat load, kW	11.3	2.9	0.113
Carnot efficiency, %	33.3	6.7	1.3
Cryoplant efficiency, %	23.0	19.3	11.3
Total power consumption, kW	147.5	224.3	76.9

D. Large-scale cooling concept and power consumption

A total of 104 wiggler systems is needed for the two CLIC damping rings. Two cooling schemes are investigated: (1) a large-scale cryogenic system connected to all wiggler magnets with cryogenic transfer lines. (2) Each wiggler magnet is independently cooled with small cryocoolers. In recent years cryocoolers have shown a considerable increase in performance, reliability and a dramatic decrease in costs.

The efficiency of large cryogenic plants can be calculated according to the Carnot efficiency [38] and with efficiency data of large-scale cryogenic plants taken from [39]. These data are in good agreement with more recent CERN experience (for example, [40]):

$$P(T_{\mathrm{op}}) \approx \frac{\frac{T_{\mathrm{op}}}{T} - 1}{\alpha C^{\beta} - \gamma} C \quad , \tag{15}$$

where $T_{\mathrm{op}} = 320$ K, $C = [10, \ldots, 10^6]$ W is the capacity of the cryoplant, and $T = [4.2, \ldots, 80]$ K the operating temperature of the cryoplant. The fitting parameters are $\alpha = 35.7$, $\beta = 0.05$, and $\gamma = 33.9$.

Table XI presents the expected power consumption of the two rings with large-scale cryogenic plants. Losses in the transfer line can be kept small, for a well-shielded line 0.05 W/m [41]. In this calculation the losses of the distribution system were considered by adding 20% to the total required heat budget.

As an alternative to a large-scale cryogenic plant, three different cryocoolers per wiggler with a total input power of around 24 kW [42], yielding a total power consumption of around 2.5 MW for the two damping rings, are proposed.

Large-scale cryogenic plants are favorable in terms of energy consumption and will consume around 5 times less electrical energy than small cryocoolers. But cryocoolers allow each wiggler to be operated independently from the others, which may increase the reliability of the CLIC damping rings. The CLIC damping rings should be designed with a certain amount of redundancy, that is, the emittance and damping time can also be met by using only a certain percentage of the damping wiggler magnets.

V. CONCLUSION

A conceptual design of superconducting damping wigglers for the CLIC damping rings was presented. Nb-Ti and Nb_3Sn superconducting CLIC damping wiggler magnets operated at 4.2 K meet the specifications. Hybrid-permanent magnet wiggler magnets cannot achieve the required magnetic fields. From the requirements of the CLIC damping rings, the gap size g, the period length λ_w, and the minimal required magnetic flux density in the center of the gap B_w of the wiggler magnets are given. Then, the choice of the wiggler coil design, the choice of the strand technology (Nb-Ti or Nb_3Sn), and the choice of the wire bundle dimension was discussed in detail in this paper. By using the presented methods and figures, the superconducting wiggler design becomes straightforward. The quench behavior is not critical, the dipole field quality in the wiggler magnets required for the damping rings can be met easily. Further, it was discussed that operation at 1.9 K is only of limited advantage and will therefore not be pursued. After showing that the magnet design of wiggler magnets for the CLIC damping rings is feasible, the design was verified by building two Nb-Ti short models, which both reached short sample current. The usage of Nb_3Sn superconductor wire may increase the midplane flux density B_w by 50%, leading to a better beam quality. However, the manufacturing of Nb_3Sn wiggler magnets is challenging due to the required heat treatment and the brittleness of the strand afterwards. The first trial coils showed that Nb_3Sn wiggler magnets are within the technological reach. The results will be published elsewhere.

The system integration of the superconducting damping wiggler was discussed in detail. Therefore, all known heat load sources from the beam and from operation are qualitatively and quantitatively discussed. Eddy currents and the heat load from resistive joints are small. The major source of heat load is beam induced. Image currents and electron clouds can be kept small, but have contradictory requirements. To reduce the electron clouds, especially in the positron ring, the beam pipe should be coated with a material with small electron emission yield, usually a material with poor conductivity. On the other hand, for the reduction of image currents the surface of the beam pipe should have high conductivity. Surface treated grooved copper requires further studies. The most important beam induced heat load is from synchrotron radiation. In this paper an optimized absorber scheme is presented with the corresponding heat load from synchrotron radiation on the beam pipes of the wiggler magnets. Further, the calculation scheme for the heat load on the beam pipes of the wiggler magnets and the absorbers is derived and presented.

The heat load study is used to discuss the cooling concept. Standard bath cooling is not an option; therefore, an advanced cooling concept is presented and conceptually derived. Two large-scale cooling concepts are presented and compared to each other. Large-scale cryogenic plants

are favorable in terms of energy consumption and will consume around 5 times less electrical energy than small cryocoolers. But cryocoolers allow independent operation of each wiggler, which may increase the reliability of the CLIC damping rings. The technical concept will be tested at the ANKA storage ring in Karlsruhe.

ACKNOWLEDGMENTS

The authors want to thank the involved members of the TE department for technical support and many valuable discussions. Special thanks are addressed to Juan Carlos Perez and Jacky Mazet for preparation of pieces and winding the CERN-KIT short-model wiggler. We want to thank Giovanna Vandoni for discussions on vacuum issues and Antonio Perin for discussions on the cryogenic system, Ezio Todesco for comments on the paper, Bernardo Bordini for performing short sample measurements, Attilio Milanese for comments on the synchrotron radiation calculation, and Emmanuele Ravaioli for PSPICE simulations. We would like to thank Denis Gurov, Anatoly Utkin, BINP, and the BINP machine shop for their support in the design and manufacturing of the CERN-BINP short model. We would like to express our gratitude to Boris Podobedov, BNL, for discussions on the image current calculations.

APPENDIX A: CALCULATION METHOD OF SYNCHROTRON RADIATION HEAT LOAD

The radiation power emitted by an electron moving on a sinusoidal trajectory is [43,44]

$$\frac{dP}{d\Omega} = \frac{d^2P}{d\theta d\psi} = 3\frac{\gamma^2}{\pi^2} P_{\mathrm{T}} f_{\mathrm{K}}(\gamma\theta, \gamma\psi), \tag{A1}$$

where θ and ψ are the observation angles in the horizontal and vertical directions (Fig. 11), and P_{T} is the total power integrated over all angles and frequencies:

$$\{P_{\mathrm{T}}\}_{\mathrm{kW}} \approx 0.633\{E\}^2_{\mathrm{GeV}}\{B_{\mathrm{w}}\}^2_{\mathrm{T}}\{L\}_{\mathrm{m}}\{I\}_{\mathrm{A}}, \tag{A2}$$

TABLE XII. Nomenclature for synchrotron radiation calculation.

Symbol	Description
a, b	1/2 of beam pipe's x and y dimension
d	Distance
d_{e}, d_z	Element size in xy and xz plane
k, l	Sequence number of wiggler and absorber
n, m	Number of elements in xy and xz plane
p	Number of downstream wigglers
r_l, s_l	1/2 of lth absorber's x and y dimension
$X_{i,j}$, $Y_{i,j}$, $Z_{i,j,k}$	Node's coordinates
θ, ψ	Angle between ray and xz and yz plane
$\theta_k^{\max}$, $\psi_k^{\max}$	Max angle of k's ray irradiating beam pipe
$\theta_{k,l}^{\max}$, $\psi_{k,l}^{\max}$	Max angle of k's ray irradiating l

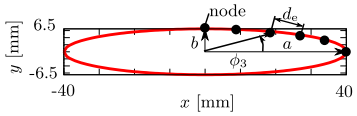

FIG. 18. Beam-pipe ellipse.

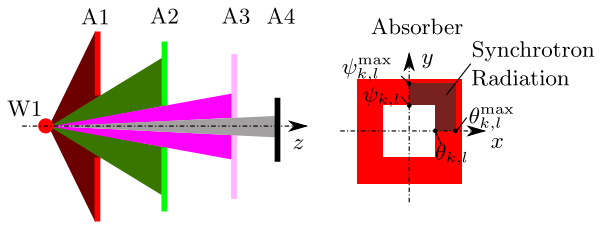

FIG. 19. Example for an absorber scheme. Left: Heat load from each wiggler magnet k (here $k = 1$) on each absorber l (here $l = 1, 2, 3, 4$). The heat load from additional wiggler magnets can be superimposed. Right: Absorber.

where L is the total length of the wiggler and I is the average current of the beam. The total dissipated power from one Nb-Ti wiggler magnet will be 14 kW.

Table XII describes the nomenclature used in the following derivation. The angular dependence is given by

$$f_{\mathrm{K}}(\gamma\theta, \gamma\psi) = \int_{-\pi}^{\pi} \sin^2\alpha\left(\frac{1}{D^3} - \frac{4(\gamma\theta - K\cos\alpha)^2}{D^5}\right)d\alpha, \tag{A3}$$

where $D = 1 + (\gamma\psi)^2 + (\gamma\theta - K\cos\alpha)^2$ and the deflection parameter K is given by

$$K = 0.934\{\lambda_{\mathrm{w}}\}_{\mathrm{cm}}\{B_{\mathrm{w}}\}_{\mathrm{T}} \approx 15.7. \tag{A4}$$

Equation (A1) cannot be integrated analytically and therefore a numerical method was developed to calculate the heat load on the beam pipe.

Figure 18 shows the cross section of the elliptic beam pipe with the axes a and b. The ellipse is divided into a mesh of $4n$ equidistant segments with a length of $d_{\mathrm{e}} = \frac{C}{4n}$ (C is the circumference of the ellipse). In the example shown in Fig. 18, n is 5. In a next step it is investigated how much radiation hits the beam-pipe segment from a downstream wiggler. In these calculations it is assumed that absorbers as shown in Fig. 19 are in position. A computer program was written to calculate the radiation generated in each longitudinal segment and also to calculate if and where the radiation hits the beam pipe. The total power deposited on the beam pipe is finally integrated and allows calculating the total deposited power on the vacuum chamber.

APPENDIX B: HEAT LOAD ON ABSORBERS

The heat load on each quadrant of the absorber l irradiated by each wiggler k can be calculated by triple numerical integration of Eq. (A1). The positive boundaries $\theta_{k,l}$

and $\psi_{k,l}$ (Fig. 19) for the calculation of the positive quadrant are given by

$$\theta_{k,l} = \arctan\frac{r_l}{d_{k,l}}, \tag{B1}$$

$$\psi_{k,l} = \arctan\frac{s_l}{d_{k,l}}, \tag{B2}$$

where $d_{k,l}$ is the distance between the wiggler k and the absorber l. The parameters r_l and s_l are the horizontal and vertical apertures of the absorber l.

The maximum angles $\theta_{k,l}^{\max}$ and $\psi_{k,l}^{\max}$ at which synchrotron radiation from wiggler k hits the absorber l is

$$\theta_{k,l}^{\max} = \min_{i=[k,l-1]} \theta_{k,i} \quad \text{with } \theta_{k,k} = \frac{\pi}{2}, \tag{B3}$$

$$\psi_{k,l}^{\max} = \min_{i=[k,l-1]} \psi_{k,i} \quad \text{with } \psi_{k,k} = \frac{\pi}{2}. \tag{B4}$$

[1] CLIC [http://clic-study.org].

[2] F. Antoniou *et al.*, in *Proceedings of the IPAC'10 Conference, Kyoto, Japan* (ICR, Kyoto, 2010), pp. 3542–3544.

[3] ANKA at Karlsruhe Institute of Technology [http://ankaweb.fzk.de].

[4] G. Rumolo *et al.*, in *Proceedings of the 11th European Particle Accelerator Conference, Genoa, 2008* (EPS-AG, Genoa, Italy, 2008), pp. 658–660.

[5] N. Mezentsev and E. Wallén, Synchrotron Radiat. News **24**, 3 (2011).

[6] P. Emma and T. Raubenheimer, Phys. Rev. ST Accel. Beams **4**, 021001 (2001).

[7] M. Korostelev, Ph.D. thesis, Ecole Polytechnique Fédérale de Lausanne, 2006.

[8] CLIC parameter list 3 TeV [http://clic-meeting.web.cern.ch/clic-meeting/clictable2010.html].

[9] F. Antoniou and Y. Papaphilippou, in Proceedings of the 11th European Particle Accelerator Conference, Genoa, 2008 (Ref. [4]), pp. 685–687.

[10] Bochvar Institute of Inorganic Materials, Moscow, Nb-Ti strand: Diameter bare 0.85 mm, insulated 0.92 mm, SC/Cu ratio 1.5/1, 630 A at 5 T, RRR 100, 330 Filaments (45 μm) [http://www.bochvar.ru].

[11] Oxford Instruments, Restacked Rod Process, diameter bare 0.81 mm, insulated 0.94 mm, SC/Cu ratio 1.1/1, 800 A at 12 T, RRR 300, 54 Filaments (80 μm) [http://www.oxinst.com].

[12] Opera Software Package, Cobham CTS Limited, 24 Bankside Kidlington Oxfordshire OX5 1JE, UK.

[13] L. Bottura, IEEE Trans. Appl. Supercond. **10**, 1054 (2000).

[14] E. Kramer, J. Appl. Phys. **44**, 1360 (1973).

[15] L. T. Summers, M. W. Guinan, J. R. Miller, and P. A. Hahn, IEEE Trans. Magn. **27**, 2041 (1991).

[16] *Insertion Devices for Rings and Linacs. IDMAX2010, Workshop, Lund, Sweden*, edited by E. Wallén (MAX-lab, Lund University, Lund, Sweden, 2010).

[17] J. Safranek *et al.*, Phys. Rev. ST Accel. Beams **5**, 010701 (2002).

[18] R. Maccaferri *et al.*, in *Proceedings of the 9th European Particle Accelerator Conference, Lucerne, 2004* (EPS-AG, Lucerne, 2004), pp. 1630–1632.

[19] B. Bordini *et al.*, IEEE Trans. Appl. Supercond. **20**, 274 (2010).

[20] D. Schoerling *et al.*, in Proceedings of the IPAC'10 Conference, Kyoto, Japan (Ref. [2]), pp. 3174–3176.

[21] CERN, LHC design report volume I. The LHC main ring (2004).

[22] C. Scheuerlein, D. Schoerling, and S. Heck, IEEE Trans. Appl. Supercond. **21**, 1791 (2010).

[23] D. Schoerling, S. Heck, C. Scheuerlein, S. Atieh, and R. Schaefer, Supercond. Sci. Technol. 25, 025006 (2012).

[24] A. B. Pippard, Proc. R. Soc. A **191**, 385 (1947).

[25] G. E. H. Reuter and E. H. Sondheimer, Proc. R. Soc. A **195**, 336 (1948).

[26] B. Podobedov, Phys. Rev. ST Accel. Beams **12**, 044401 (2009).

[27] G. Rumolo, F. Ruggiero, and F. Zimmermann, Phys. Rev. ST Accel. Beams **4**, 012801 (2001).

[28] D. Alesini, CERN Accelerator School, 2010.

[29] Y. Suetsugu *et al.*, in Proceedings of the IPAC'10 Conference, Kyoto, Japan (Ref. [2]), pp. 2021–2023.

[30] M. A. Palmer *et al.*, in Proceedings of the IPAC'10 Conference, Kyoto, Japan (Ref. [2]), pp. 1251–1255.

[31] H. Wiedemann, *Particle Accelerator Physics* (Springer, Berlin, 2007).

[32] NISTIR 5632 [http://www.nist.gov/physlab/data/xraycoef/index.cfm].

[33] W. Fastowski, J. Petrowski, and A. Rowinski, *Kryotechnik* (Akademie Verlag, Berlin, 1970).

[34] H. Frey and R. Haefer, *Tieftemperaturtechnik* (VDI-Verlag, Düsseldorf, 1981).

[35] Y. Iwasa, *Case Studies in Superconducting Magnets* (Springer, New York, 2009).

[36] P. Lebrun, Report No. CERN-2004-008, 2004.

[37] G. Vandoni, Report No. CERN-2004-008, 2004.

[38] R. Barron, *Cryogenic Systems* (Oxford Science Publications, New York, 1985).

[39] T. Strobridge, Cryogenic Refrigerators—An Updated Survey, NBS Technical Note No. 655 (U.S. GPO, Washington, DC, 1974).

[40] S. Claudet *et al.*, Technical Report No. LHC-Project-Report-317, 1999.

[41] A. Perin (private communication).

[42] Three cryocoolers are used: (1) Cryomech Al325 [http://cryomech.com], (2) SHI cryogenic groups CH-210, and (3) RDK-415D [http://www.shicryogenics.com].

[43] J. Schwinger, Phys. Rev. **75**, 1912 (1949).

[44] K.-J. Kim, Nucl. Instrum. Methods Phys. Res., Sect. A **246**, 67 (1986).

[45] R. Tomás, Phys. Rev. ST Accel. Beams **13**, 014801 (2010).

[46] NIST Cryogenic material properties website [http://www.cryogenics.nist.gov].